

Unzueta, Iraultza; Gunnlaugsson, Haraldur Pall; Mølholt, Torben Esmann; Masenda, Hilary; Gerami, Adeleh Mokhles; Krastev, Petko; Zyabkin, Dmitry; Bharuth-Ram, Krish; Naidoo, Deena; Ólafsson, Sveinn; Plazaola, Fernando; Schell, Juliana; Qi, Bingcui; Zhao, Xupeng; Xiao, Jiaying; Zhao, Jianhua; Mantovan, Roberto

**Compositional dependence of epitaxial L10-Mnx Ga magnetic properties as probed by 57Mn/Fe and 119In/Sn emission Mössbauer spectroscopy**

---

*Original published in:* Physica status solidi. B. - Weinheim : Wiley-VCH. - 259 (2022), 7, art. 2200121, 11 pp.  
*Original published:* 2022-04-23  
*ISSN:* 1521-3951  
*DOI:* [10.1002/pssb.202200121](https://doi.org/10.1002/pssb.202200121)  
*[Visited:* 2022-10-21]



This work is licensed under a [Creative Commons Attribution 4.0 International license](https://creativecommons.org/licenses/by/4.0/). To view a copy of this license, visit <https://creativecommons.org/licenses/by/4.0/>

# Compositional Dependence of Epitaxial $L1_0$ - $Mn_xGa$ Magnetic Properties as Probed by $^{57}Mn/Fe$ and $^{119}In/Sn$ Emission Mössbauer Spectroscopy

*Iraultza Unzueta,\* Haraldur Pall Gunnlaugsson, Torben Esmann Mølholt, Hilary Masenda, Adeleh Mokhles Gerami, Petko Krastev, Dmitry V. Ziyabkin, Krish Bharuth-Ram, Deena Naidoo, Sveinn Ólafsson, Fernando Plazaola, Juliana Schell, Bingcui Qi, Xupeng Zhao, Jiaying Xiao, Jianhua Zhao, and Roberto Mantovan\**

The magnetic properties of  $Mn_xGa$  alloys critically depend on composition  $x$ , and the atomic-scale origin of those dependences is still not fully disclosed. Molecular beam epitaxy has been used to produce a set of  $Mn_xGa$  samples ( $x = 0.7 \div 1.9$ ) with strong perpendicular magnetic anisotropy, and controllable saturation magnetization and coercive field depending on  $x$ . By conducting  $^{57}Mn/Fe$  and  $^{119}In/Sn$  emission Mössbauer spectroscopy at ISOLDE/CERN, the Mn and Ga site-specific chemical, structural, and magnetic properties of  $Mn_xGa$  are investigated as a function of  $x$ , and correlated with the magnetic properties as measured by superconducting quantum interference device magnetometry. Hyperfine magnetic fields of Mn/Fe (either at Mn or Ga sites) are found to be greatly influenced by the local strain induced by the implantation. However, In/Sn probes show clear angular dependence, demonstrating a huge transferred dipolar hyperfine field to the Ga sites. A clear increase of the occupancy of Ga lattice sites by Mn for  $x > 1$  is observed, and identified as the origin for the increased antiferromagnetic coupling between Mn and Mn at Ga sites that lowers the samples' magnetization. The results shed further light on the atomic-scale mechanisms driving the compositional dependence of magnetism in  $Mn_xGa$ .


## 1. Introduction

Magnetic materials exhibiting high perpendicular magnetic anisotropy (PMA) in combination with high spin polarization,<sup>[1]</sup> high Curie temperature ( $T_C$ ), and tuneable magnetization are the most ideal candidates for spin-based memory or logic devices.<sup>[2,3]</sup> In this context, one of the most studied systems are Ta/ultrathin CoFeB/MgO-based heterostructures, where the PMA is obtained via the CoFeB/MgO interface anisotropy.<sup>[4–7]</sup> The effective anisotropy constant  $K_u^{eff}$ , which ultimately determines the thermal stability of a memory cell, can be improved by engineering appropriate CoFeB-based heterostructures. On the other hand, these heterostructures become thermally unstable when lateral dimensions are scaled below 30 nm.<sup>[8]</sup> Thus, single magnetic thin films displaying high PMA and  $K_u^{eff}$  are an interesting solution to ensure the required thermal stability

for applications in several spintronic devices. A special class of binary Heusler alloys such as  $Mn_xGa$  are leading candidates.

I. Unzueta  
Department of Applied Mathematics  
University of the Basque Country UPV/EHU  
48013 Bilbao, Spain  
E-mail: iraultza.unzueta@ehu.eus

H. P. Gunnlaugsson, S. Ólafsson, B. Qi  
Science Institute  
University of Iceland  
Dunhaga 3, IS-107 Reykjavík, Iceland

 The ORCID identification number(s) for the author(s) of this article can be found under <https://doi.org/10.1002/pssb.202200121>.

© 2022 The Authors. physica status solidi (b) basic solid state physics published by Wiley-VCH GmbH. This is an open access article under the terms of the Creative Commons Attribution License, which permits use, distribution and reproduction in any medium, provided the original work is properly cited.

DOI: 10.1002/pssb.202200121

T. E. Mølholt  
EP Department  
ISOLDE/CERN  
1211 Geneva 23, Switzerland

H. Masenda, D. Naidoo  
School of Physics  
University of the Witwatersrand  
Johannesburg 2050, South Africa

H. Masenda  
Faculty of Physics and Materials Sciences Center  
Philipps-Universität Marburg  
35032 Marburg, Germany

A. Mokhles Gerami  
School of Particles and Accelerators  
Institute for Research in Fundamental Sciences (IPM)  
P.O. Box 19395-5531, Tehran, Iran

Apart from their potential use as rare-earth-free permanent magnets,<sup>[9,10]</sup> they have also attracted high interest for application in high-density PMA-based magnetic random-access memories driven by spin-transfer torque or spin-orbit torque<sup>[10–13]</sup> because their room temperature (RT) thermal stability can be achieved in magnetic bits sized-down to less than 5 nm.<sup>[9]</sup> Indeed, the inclusion of Mn<sub>x</sub>Ga in PMA magnetic tunnel junctions and spin-orbit torque magnetic tunnel junctions has been demonstrated.<sup>[14,15]</sup>

Mn<sub>x</sub>Ga films crystallize in the tetragonal *L*<sub>10</sub> ( $x < 2$ ) and *D*<sub>022</sub> ( $2 < x < 3$ ) structures, giving rise to strong magnetocrystalline anisotropy with magnetically easy axis parallel to *c* axis.<sup>[16]</sup> While *D*<sub>022</sub> structure is a ferrimagnetic ordered phase,<sup>[1,17,18]</sup> *L*<sub>10</sub> structure is a ferromagnetic (FM) phase for  $0.76 < x < 1.9$ .<sup>[16,19,20]</sup> *L*<sub>10</sub>-type MnGa belongs to a *P4/mmm* space group where lattice constants range between  $a = 3.88\text{--}3.90$  and  $c = 3.64\text{--}3.69$  Å,<sup>[16,19]</sup> and exhibits high Curie temperature (*T*<sub>c</sub>) and spin polarization, together with a large magnetic anisotropy and coercive field (*H*<sub>c</sub>).

Very interestingly, Zhu et al.<sup>[10]</sup> showed that in Mn<sub>x</sub>Ga ( $0.76 < x < 2.6$ ) thin films, appropriate postgrowth annealing processing is efficient for varying the saturation (*M*<sub>s</sub>) and remanence (*M*<sub>r</sub>) magnetizations, the magnetic energy product, and the *H*<sub>c</sub>. The compositional dependence of magnetic properties of Mn<sub>x</sub>Ga compounds is an interesting route to tune the properties of these alloys, thus optimizing their performances in the specific target application. In particular, the largest variation of the Mn<sub>x</sub>Ga magnetic properties appears to take place within the compositional range  $0.76 < x < 1.75$ .<sup>[21]</sup> By varying Mn content and/or the postgrowth annealing treatments, the *M*<sub>r</sub>/*M*<sub>s</sub> ratio increases as Mn content increases, exceeding the 0.9 value at  $x = 1.75$ . The magnetic anisotropy increases along with *x* in this range, which seems to correlate with the induced variation of the *H*<sub>c</sub>. However, the lattice constant *c* decreases as *x* increases. This fact reveals the strong interplay between the structure/strain and the magnetic properties in this system. Thus, the control of the composition, structure, strains, and the growth temperature during the synthesis process plays a key role in optimizing the magnetic properties.<sup>[9]</sup>

The primary objective of the present work is to ascertain the microscopic origin of the observed dependence of macroscopic

magnetic properties with the stoichiometry of Mn<sub>x</sub>Ga and the thermal history to which they are subjected. Within this objective, we employ <sup>119</sup>Sn and <sup>57</sup>Fe emission Mössbauer spectroscopy (eMS) conducted at the radioactive large-scale ion beam facility at ISOLDE/CERN, which has proved to be a powerful method to investigate chemical, structural, and magnetic properties at the atomic scale, in a very dilute implantation regime.<sup>[22–25]</sup> The unique sensitivity of eMS to tiny structural changes (e.g., induced by the strain during synthesis process) makes possible the study of the correlation between macro- and micro-scaled properties.

Currently, limited reports exist on Mössbauer spectroscopy (MS) studies of Mn<sub>x</sub>Ga thin films, due mainly to the fact that neither Mn nor Ga atoms are Mössbauer-active elements. Betto et al.<sup>[5]</sup> performed <sup>57</sup>Fe-MS in Fe-doped Mn<sub>2</sub>Fe<sub>x</sub>Ga thin films, where a clear magnetic contribution arises attributed to ordered out-of-plane Fe<sup>3+</sup>. Koeba et al.<sup>[26]</sup> also carried out <sup>57</sup>Fe-MS in Fe-doped *D*<sub>022</sub> Mn<sub>3–x</sub>Fe<sub>x</sub>Ga alloys, but on powdered samples. By conducting eMS at ISOLDE/CERN, we make use of implantation of radioactive <sup>57</sup>Mn (<sup>119</sup>In) ions, decaying to the <sup>57</sup>Fe (<sup>119</sup>Sn) Mössbauer state, thus providing opportunities to explore the Mn<sub>x</sub>Ga properties through eMS at substitutional cationic Mn and anionic Ga sites, while keeping chemically unperturbed the original Mn<sub>x</sub>Ga layers, at the adopted ultradiluted regime.

Contrary to expectations, our results demonstrate that the <sup>119</sup>Sn nuclei at Ga sites are much more sensitive to the volume magnetism of the Mn<sub>x</sub>Ga samples than the <sup>57</sup>Fe probes at Mn sites. Although the evolution of the hyperfine fields revealed by <sup>57</sup>Mn/Fe-eMS correlate with macroscopic magnetic properties of Mn<sub>x</sub>Ga samples, strains and slight atomic distortions have a great impact on the Mn–Mn coupling, making <sup>57</sup>Mn/Fe-eMS very sensitive to the strain state. On the other hand, even under the presence of strong distortions induced by implantation, <sup>119</sup>In/Sn-eMS reveal huge magnetic contribution at Ga sites, as it is corroborated by angular dependence measurements. The total transferred hyperfine field from polarized *d* conduction electrons of Mn ions at <sup>119</sup>Sn nuclei at Ga sites is found to be less sensitive to the distortions and local strains, which turns <sup>119</sup>Sn into an efficient Mössbauer probe to study the magnetic properties of Mn<sub>x</sub>Ga alloys.

P. Krastev  
Institute for Nuclear Research and Nuclear Energy  
Bulgarian Academy of Sciences  
Tsarigradsko Chaussee Boulevard, 1784 Sofia, Bulgaria

D. V. Zybkin  
Chair Materials for Electronics  
Institute of Materials Science and Engineering  
Institute of Micro and Nanotechnologies MacroNano  
TU Ilmenau  
98693 Ilmenau, Germany

K. Bharuth-Ram  
School of Chemistry and Physics  
University of KwaZulu-Natal  
Durban 4001, South Africa

K. Bharuth-Ram  
South Africa Physics Department  
Durban University of Technology  
Durban 4000, South Africa

F. Plazaola  
Department of Electricity & Electronics  
University of the Basque Country UPV/EHU  
48013 Leioa, Spain

J. Schell  
Institute for Materials Science and Center for Nanointegration Duisburg-Essen (CENIDE)  
University of Duisburg-Essen  
45141 Essen, Germany

X. Zhao, J. Xiao, J. Zhao  
State Key Laboratory of Superlattices and Microstructures  
Institute of Semiconductors  
Chinese Academy of Sciences  
P.O. Box 912, Beijing 100083, China

R. Mantovan  
CNR-IMM  
Unit of Agrate Brianza  
Via Olivetti 2, 20864 Agrate Brianza (MB), Italy  
E-mail: roberto.mantovan@mdm.imm.cnr.it

## 2. Experimental Section

A series of  $L1_0$ - $Mn_xGa$  films of 120 nm thick with different Mn/Ga atom ratio  $x$  ( $x = 0.7, 0.8, 1.1, 1.4, 1.9$ ), all 120 nm thick, were grown using molecular beam epitaxy (MBE) following codeposition of Mn and Ga at the growth temperature of 523 K on 150 nm GaAs-buffered semi-insulating GaAs (001) substrate. All the  $Mn_xGa$  layers are capped with 2 nm Al layer to prevent oxidation (see **Figure 1**). The base pressure was kept at  $10^{-9}$  mbar.

The composition  $x$  of the synthesized samples was controlled by monitoring Mn and Ga fluxes. Reflection high energy electron diffraction (RHEED) was applied to in situ monitor the surface reconstruction during growth. For all samples, superconducting quantum interference device (SQUID) magnetometry measurements were conducted prior to eMS with a Quantum Design QD MPMS XL-5 magnetometer with applied magnetic fields up to 5 T (see Section 3.1).

$^{57}Fe$ -eMS and  $^{119}Sn$ -eMS measurements were carried out at the ISOLDE facility at CERN. Radioactive  $^{57}Mn$  ( $t_{1/2} = 1.4$  min) and  $^{119}In$  ( $t_{1/2} = 2.4$  min) ions were produced by 1.4 GeV

proton-induced fission of heated  $UC_2$  target, which are desorbed and ionized with elemental selective multiphoton laser ionization processes.<sup>[27–29]</sup> The ionized  $^{57}Mn$  and  $^{119}In$  isotopes were then accelerated at 50 keV, and by means of magnetic fields pure  $^{57}Mn$  and  $^{119}In$  beams of  $\approx 10^8$  ions  $(cm^2 s)^{-1}$  in intensity were obtained. Each spectrum was recorded during an average 5 min concurrent implantation/measurement time with a maximum estimated implantation fluence of  $10^{12}$  at  $cm^{-2}$ , thus ensuring the dilute concentration regime (corresponding to  $\approx 10^{-4}$  at.%) and avoiding overlapping damage cascades, which typically occurs above  $10^{13}$ – $10^{14}$  at.  $cm^{-2}$ .<sup>[22]</sup> Isomer shifts are given relative to the center of  $\alpha$ -Fe spectrum at RT (for  $^{57}Mn/Fe$ -eMS) and relative to  $SnO_2$  (for  $^{119}In/Sn$ -eMS). The recorded eMS spectra have been analyzed with the VINDA software package.<sup>[30]</sup> A close look of the eMS setup at the end of the ISOLDE beamline is depicted in **Figure 2**.

Samples are implanted at an incident angle  $\theta_i = 30^\circ$ , with the  $c$ -axis (surface normal  $\hat{n}$ ) relative to the beam direction. The detector is placed at  $\theta_e = 60^\circ$  relative to  $\hat{n}$  and at  $90^\circ$  relative to the beam direction, so that  $\theta_i + \theta_e = 90^\circ$ . In this work, two

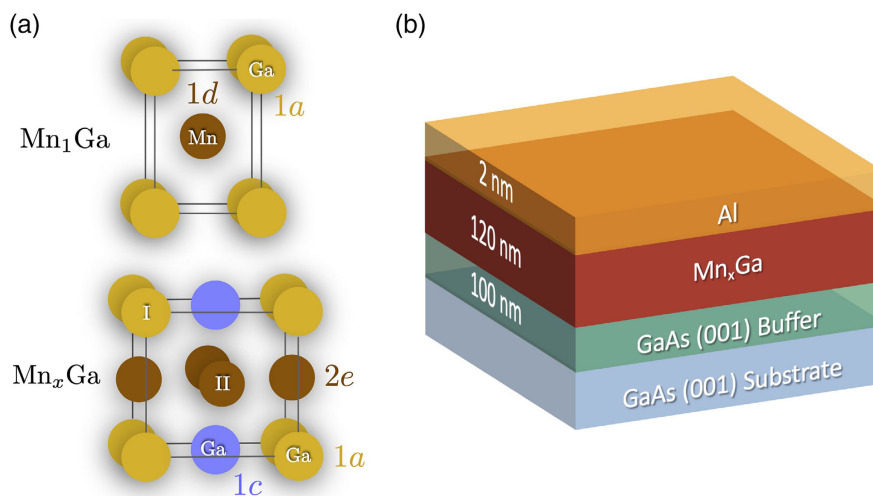


**Figure 1.** a) Crystal structure of  $L1_0$  structure of  $Mn_xGa$  samples in stoichiometric ( $x=1$ , top) and off-stoichiometric ( $x \neq 1$ , bottom) conditions. b) Schematic layered arrangement of the  $Mn_xGa$  films.

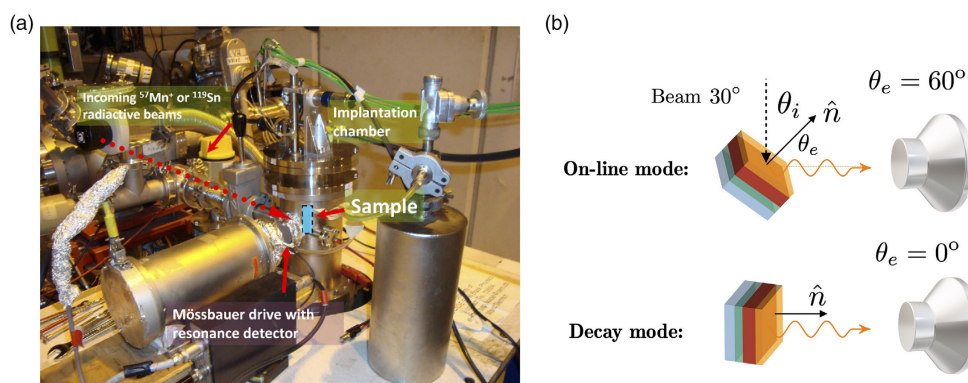


**Figure 2.** a) Arrangement of the sample, detector, and the beamline of the eMS experiments at ISOLDE/CERN. b) Schematics of the two measuring modes used in the temperature series (online mode) and in the angular-dependent measurements (decay mode).

different methods were applied: 1) the so-called online mode in which the sample is implanted while measuring at  $\theta_e = 60^\circ$  (see Figure 1b); and 2) the decay mode in which the sample is first implanted and measured at  $\theta_e = 60^\circ$  for 180 s, and then rotated to  $\theta_e = 0^\circ$  where the decay radiation is collected for 240 s.<sup>[31]</sup> The decay mode has been used mainly for angular dependence experiments. This procedure is repeated up to 4 times to assure high statistics spectra.

### 3. Results and Discussion

#### 3.1. Magnetic Characterization

Figure 3 shows the SQUID data for all the samples. The extracted  $M_s$  and  $H_c$  are all gathered in Table 1, together with the available  $T_c$  values from the literature. A clear decrease of  $M_s$  and increase of  $H_c$  are detected with increasing the Mn content  $x$ . Such trends, for both  $M_s$  and  $H_c$ , are in very good agreement with those previously reported for a similar set of samples.<sup>[10]</sup> The observed decrease of  $M_s$  with  $x$  is tentatively attributed to enhance antiferromagnetic (AF) coupling between neighboring Mn atoms.<sup>[10]</sup> Furthermore, site occupation in the  $L1_0$  lattice also has a prominent impact on the magnetic properties of the system.<sup>[9]</sup> Theoretical calculations on the effect of strains show that the magnetic structures and the lattice parameters are greatly affected,<sup>[32]</sup> resulting in a smaller magnetic moment. Thus, in

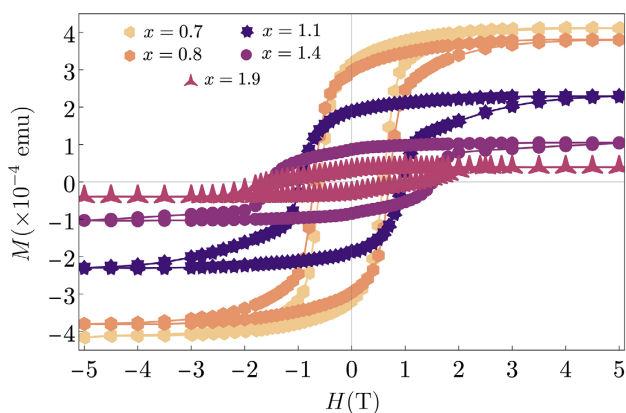


Figure 3. SQUID measurements of  $M(H)$  curves applied up to 5 T for all the studied samples.

Table 1. Composition  $x$ ,  $M_s$ ,  $H_c$ , and  $T_c$  (when available) for all the  $Mn_xGa$  samples studied in the article.

Structure	$M_s$ [ $\mu_B \text{ cm}^{-3}$ ]	$H_c$ [Oe]	$T_c$ [K]
$Mn_{0.7}Ga$	214.06	5914	>300
$Mn_{0.8}Ga$	198.10	7059	>300
$Mn_{1.1}Ga$	119.16	9571	595 <sup>a)</sup>
$Mn_{1.4}Ga$	54.10	15195	630 <sup>b)</sup> , 625 <sup>c)</sup> , 680 <sup>a)</sup>
$Mn_{1.9}Ga$	20.46	14920	700 <sup>c)</sup> , 740 <sup>a)</sup>

a) Ref.<sup>[33]</sup> b) Ref.<sup>[10]</sup> c) Ref.<sup>[34]</sup>

$Mn_xGa$  samples both the lattice strains and Mn content primarily govern the magnetic moment of Mn atoms.

#### 3.2. $^{57}Mn/Fe$ eMS

The main focus of the present study is to get insights into the connection between the change in the macroscopic magnetism observed in the series of  $Mn_xGa$  ( $x = 0.7, 0.8, 1.1, 1.4, 1.9$ ) samples (Figure 3), with the corresponding atomic-scale structure and magnetic properties as investigated by eMS.

All the  $Mn_xGa$  samples were initially implanted below RT, at temperatures low enough to clearly observe the implantation-induced damage component. This is a necessary strategy in order to precisely identify such a contribution, being then able to follow its evolution with temperature. However, the spectra obtained on samples implanted above RT do not show the implantation-induced damage component.<sup>[35–38]</sup> Details are presented in Section S1, Supporting Information.

Figure 4 and 5 show the  $^{57}Mn/Fe$ -eMS data recorded in the 298–678 and 300–676 K temperature ranges for the  $Mn_{1.1}Ga$  and  $Mn_{0.7}Ga$  samples, respectively. Both series are measured at  $60^\circ$  in online mode (see Figure 2b).

All spectra show a central broad emission line around velocities of  $0 \text{ mm s}^{-1}$ . A characteristic additional broadening related to magnetic component can be seen at the wings, as clearly evinced in  $Mn_{1.1}Ga$  sample measured at 583 K (see Figure 4). Moreover, the spectra of  $Mn_{0.7}Ga$  taken at 300 K (see Figure 5) show that the central component is indeed composed of a “doublet” with moderate quadrupole splitting ( $\approx 0.5 \text{ mm s}^{-1}$ ). As will be justified later, this doublet component, which contributes significantly even well below  $T_c$ , is compatible with the contribution of paramagnetic  $^{57}Fe$  ions in regions with an altered magnetic order caused by the implantation induced stresses–strains.

Although in the composition range studied in this work,  $Mn_xGa$  should crystallize in the  $L1_0$  phase, the off-stoichiometry and chemical disorder often present in these samples allow the structure to be described by  $L1_0$  and  $D0_{22}$  phases.<sup>[11,39]</sup> As shown in Figure 1a, in the stoichiometric  $Mn_1Ga$  compound, Mn and Ga atoms occupy the  $1d$  and  $1a$  Wyckoff positions, respectively. Mn atoms contribute to the magnetism with  $2.51 \mu_B$ , while Ga atoms contribute with a negligible atomic moment to the macroscopic magnetism.<sup>[11,39]</sup> However, in the off-stoichiometric conditions, the Mn atoms reside in  $2e$  Wyckoff position while the exceeded Mn atoms tend to occupy the natural Ga  $1a$  and  $1c$  positions, which increases the AF coupling between neighboring Mn atoms, thus lowering the overall magnetism as the Mn content increases.<sup>[39,40]</sup> The magnetic moments of Mn atoms which occupy Ga positions are larger than and antiparallel ( $\approx 3 \mu_B/\text{Mn}$ ) to those Mn in their natural positions ( $\approx 2.45 \mu_B/\text{Mn}$ ).<sup>[4,26,39]</sup> Thus, due to the different atomic environments of the  $Mn_I$  and  $Mn_{II}$  positions (see Figure 1a) in  $Mn_xGa$  samples, different isomer shift have been used for the two sextets.<sup>[26]</sup> To the extent possible, the isomer shift values allowed to follow the so-called second-order Doppler shift (SODS) with rising temperature.

In  $^{57}Fe$ -eMS experiments, the implanted Mn ions could be initially located at both natural Mn and Ga positions or interstitially.



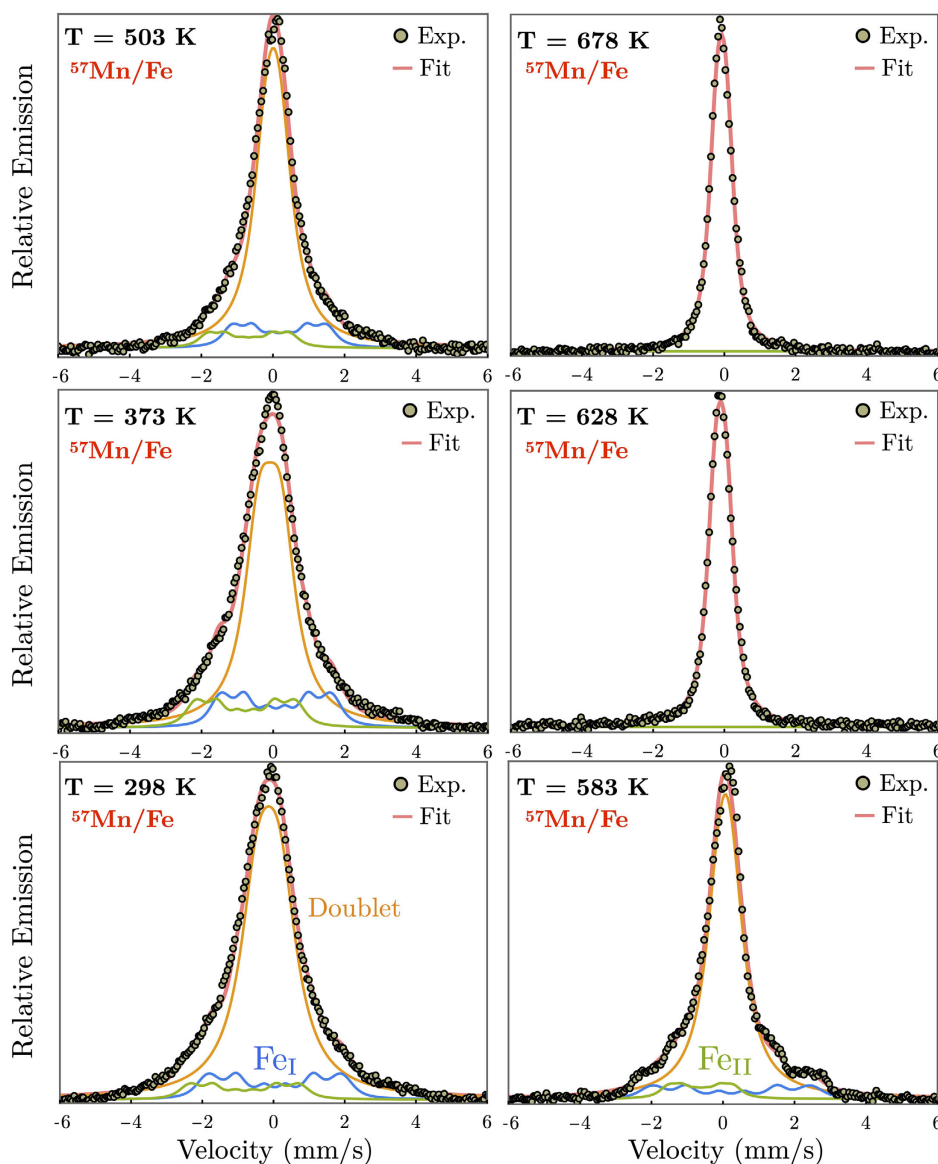


**Figure 4.**  $^{57}\text{Fe}$ -eMS measurements for  $\text{Mn}_{1.1}\text{Ga}$  samples within the 298–678 K temperature range.

The interstitial sites are characterized with a lower Debye temperature compared to substitutional sites<sup>[37]</sup> and a vanishing component as a function of increasing temperature typically reveals the interstitial character of the identified contributions. Analysis of the whole set of temperature-dependent data for the samples listed in Table 1 does not provide any evidence for such component nor of the presence of Mn/Fe fractions in interstitial sites in all spectra taken above RT. Thus, at temperatures above it, it can be considered that all implanted Mn atoms occupy substitutional sites.

However, given the scarce features revealed by the eMS spectra measured in both Mn-deficient (e.g.,  $\text{Mn}_{0.7}\text{Ga}$  in Figure 5) and Mn-rich (e.g.,  $\text{Mn}_{1.1}\text{Ga}$  in Figure 4) samples, the fitting for all the studied  $\text{Mn}_x\text{Ga}$  samples was determined, as well, based on previously existing Mössbauer data<sup>[26]</sup> and on the crystal

structure of  $\text{Mn}_x\text{Ga}$  alloys. As a result, the following three different components have been used: 1) a sextet component for Mn/Fe in natural  $\text{Mn}_{\text{II}}$  positions ( $\text{Fe}_{\text{II}}$ ); 2) a sextet component for the excess of Mn/Fe atoms occupying natural Ga sites in  $\text{Mn}_{\text{I}}$  ( $\text{Fe}_{\text{I}}$ ); and 3) a doublet component given the tetragonal structure of the  $\text{Mn}_x\text{Ga}$  films and comprising the contribution  $^{57}\text{Fe}$  atoms located at nonmagnetic substitutional sites. The spectral lines were fitted with Voigt line shapes. Moreover, the isomer shift  $\delta$  has been constrained to follow the SODS with  $\Theta_{\text{D}} \approx 500$  K, which increases with increasing the Mn content.<sup>[41]</sup> Although fits with better chi-squares could be obtained by using different fitting methods (e.g., hyperfine field distributions), the adopted procedure gave the most reliable trend of the hyperfine parameters.

An important feature clearly emerging in both Figure 4 and 5 is that all the spectra become narrower as temperature increases,

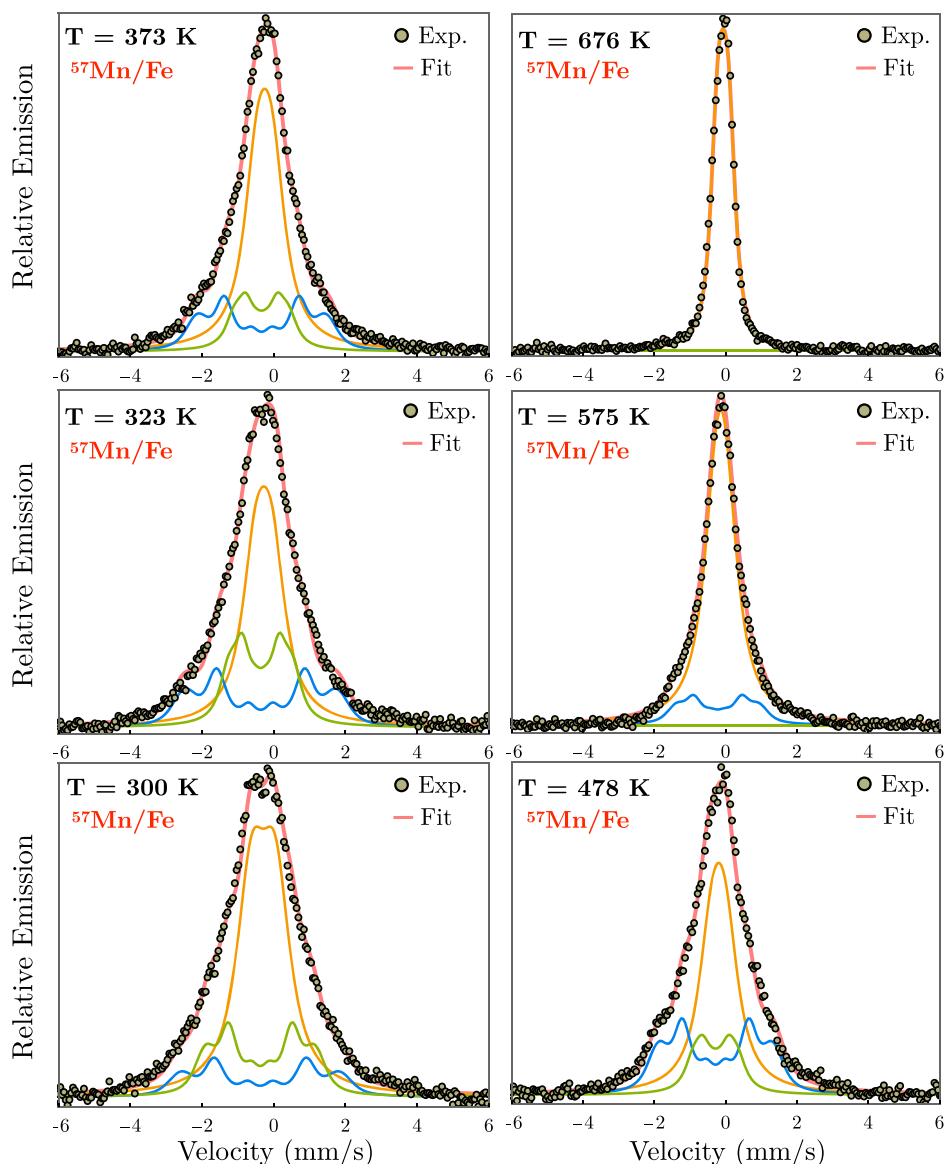


**Figure 5.**  $^{57}\text{Fe}$ -eMS measurements for  $\text{Mn}_{0.7}\text{Ga}$  samples within the 300–676 K temperature range.

with the highest temperature data that can be satisfactorily fitted with a single doublet component. This is related to the gradual approach to  $T_c$ , which is in the range of 600–750 K (see Table 1). However, the important contribution of the doublet component even well below  $T_c$  can be understood as the presence of paramagnetic  $^{57}\text{Fe}$  ions due to altered FM order in the very close environment caused by the implantation. The overall trend of the hyperfine parameters observed for the remaining samples  $\text{Mn}_x\text{Ga}$  ( $x = 0.8, 1.4$  and  $1.9$ ) is similar to those observed for  $\text{Mn}_{0.7}\text{Ga}$  and  $\text{Mn}_{1.1}\text{Ga}$  samples (see Section S2, Supporting Information).

The temperature evolution of the hyperfine parameters obtained from the fitting of experimental spectra is gathered in **Figure 6**, which summarizes the composition and temperature dependences of the  $B_{\text{hf}}$  for (a)  $\text{Mn}_{\text{II}}$ , (b)  $\text{Mn}_{\text{I}}$ , (c) their

corresponding isomer shift, (d) the hyperfine parameters related to the quadrupole splitting, and (e) the relative area fractions of all the components. The RT values of all the spectral components are summarized in Table S1, Supporting Information.

The trend that the three spectral intensities follow over the temperature range is similar for all the studied samples (see Figure 6e). At RT, the component which contributes most is the doublet component. Taking into account the related isomer shift values, it can be attributed to a paramagnetic  $\text{Fe}^{3+}$  atoms, which, due to the presence of internal stresses/strains and the altered magnetic order, do not exhibit magnetic splitting.<sup>[5]</sup> The two sextets, however, correspond to ordered out-of-plane metallic Fe. These last two magnetic components from  $\text{Fe}^{3+}$  contribute less than 40% in overall. The area fractions of these two components decrease quite monotonically as the temperature

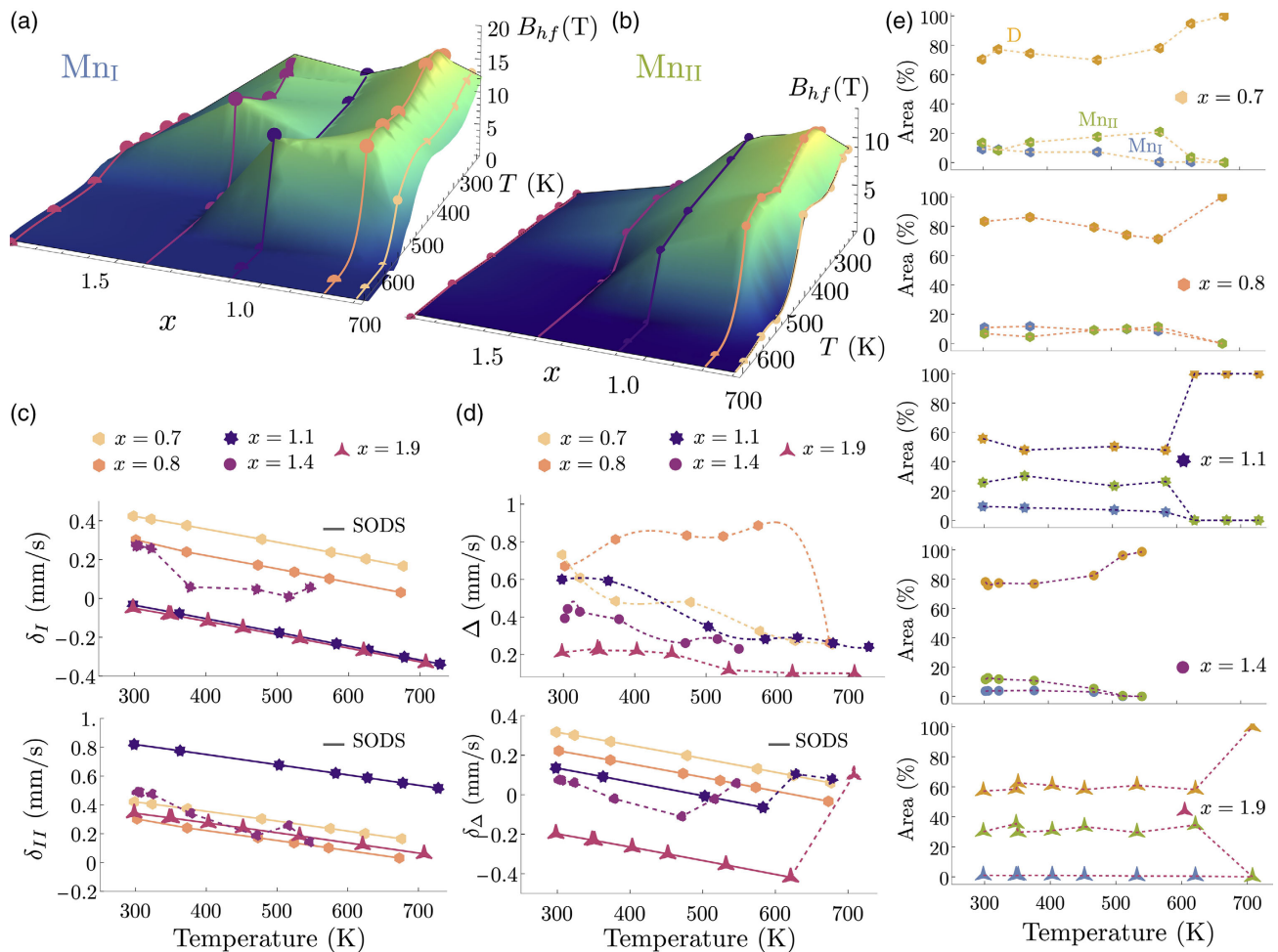


**Figure 6.** Evolution of the hyperfine field as a function of composition and temperature of a)  $Mn_I$  and b)  $Mn_{II}$  sites. c) Temperature dependence of the isomer shift values for the two sextets of  $Mn_I$  ( $\delta_I$ ) and  $Mn_{II}$  ( $\delta_{II}$ ) sites. The dashed line is a guide to eye, while the solid line represents the SODS. d) Temperature evolution of the quadrupole splitting component and isomer shift. e) Area fractions of the three spectral components for all the studied samples. The errors of the hyperfine parameters are shown in Table S1, Supporting Information.

approaches  $T_c$  (without considering the small enhancements that occur due to the annealing of the implantation induced stresses/strains). Above it, the contribution of magnetic  $Fe^{3+}$  vanishes and the spectra are fitted with a single doublet component.

The comparison between Figure 6a,b shows that the hyperfine field values at  $Mn_I$  sites are higher than those of  $Mn_{II}$  sites (see Table S1, Supporting Information), which is consistent with previous reports.<sup>[4,26]</sup> The Mn atoms occupying the natural Ga sites are characterized for having a larger magnetic moment comparing with the Mn atoms located at  $2e$  sites. Both observed hyperfine fields collapse fairly monotonically with rising temperature. At temperatures close to  $T_c$ , all spectra can only be fitted with a single doublet component. The obtained  $T_c$  values lie between 600 and 750 K, in a good agreement with values reported in the literature, within the studied composition range (see Table 1).<sup>[34]</sup> Moreover, with increasing the Mn content  $x$ , the  $B_{hf}$  values at both  $Mn_I$  and  $Mn_{II}$  decrease, in accordance with the overall decrease of  $M_s$  (see Figure 3). This effect is attributed to the exceeded Mn atoms placed at both  $1a$  and  $1c$  sites, coupling

antiferromagnetically to those in  $2e$  positions, and hence resulting in the decrease of the saturation magnetization of  $Mn_xGa$  alloys.<sup>[10]</sup> At the most atomic scale, the  $^{57}Mn$ -eMS data enable to separately follow the  $x$ -dependence of the local magnetic field at the two sites, and a faster decrease of  $B_{hf}$  with increasing  $x$  is observed at the Mn lattice site when compared to that at the Ga lattice site (i.e., see Figure 6a,b at a fixed temperature of 300 K). This shows the relevant role played in the  $x > 1$  samples by the local magnetic moments at Ga sites in tuning the macroscopic magnetism of the  $Mn_xGa$  alloys.

Interestingly, within the 400–500 K temperature range, and prior to reach  $T_c$ , the hyperfine field values of both the  $Mn_I$  and  $Mn_{II}$  components reach a maximum. We attribute this slight enhancement to the partial lattice damage annealing occurring in the  $Mn_xGa$  layers. Although the implantation damage is negligible  $> RT$  (see Figure S1, Supporting Information), this does not rule out the implantation-induced internal stresses/strains which would modify slightly the very close structural environment of the  $^{57}Mn/Fe$  probe atom. Indeed, within the Bethe–Slater and



Ruderman–Kittel–Kasuya–Yosida (RKKY) exchange interaction models, it is well known that the variation in Mn–Mn distances can induce the magnetic coupling of Mn ions to become from FM to AF. This has been observed in Ni–Mn–Ga ternary alloys, very similar to those of Mn–Ga as far as the magnetic interaction is concerned.<sup>[42]</sup> A similar effect is also observed in other Ni-based Heusler alloys by means of <sup>119</sup>Sn MS, where the annealing of the strains is closely related with the observed magnetic splitting in Mössbauer spectra.<sup>[43–45]</sup> As a result, the recovery of the internal stresses and strains has a major impact on the measured hyperfine parameters in Mn<sub>x</sub>Ga alloys.

Although with increasing temperature the hyperfine field value should decrease (due to the proximity to  $T_c$ ), this apparent increase of  $B_{hf}$  in the 400–500 K range exactly denotes such a structural recovery/annealing of stresses/strains taking place within this temperature interval. Taking into account that the magnetism of Mn<sub>x</sub>Ga alloys is sensitive to the presence of strains with a direct impact on the  $M_s$  and  $M_r$ ,<sup>[9,10]</sup> our results show how <sup>57</sup>Mn/Fe-eMS can assess the local strain state of Mn<sub>x</sub>Ga samples.

Figure 6c shows the temperature evolution of the isomer shift related to the Mn<sub>I</sub> ( $\delta_I$ ) and Mn<sub>II</sub> ( $\delta_{II}$ ) sites for all the studied samples. For samples  $x = 0.7, 0.8, 1.1,$  and  $1.9$ , the isomer shift of two magnetic components follows the SODS (solid line), decreasing the value as the temperature increases. However, for the  $x = 1.4$  sample, the isomer shift values do not follow the SODS. The different evolution in terms of SODS consistency could be due the presence of crystal imperfections and formation of phases with slightly altered orientations, which also explains the huge increase that  $H_c$  experiences from the  $x = 1.1$  sample to  $x = 1.4$  sample.<sup>[46,47]</sup> For all samples, the isomer shifts are mainly bounded between  $|\delta_{D,I,II}| < 0.5 \text{ mm s}^{-1}$ , compatible with FM (sextet) and paramagnetic Fe<sup>3+</sup> (doublet) configuration.<sup>[4]</sup>

As shown in Figure 5d, a similar trend is observed for the isomer shift related to the doublet component ( $\delta_\Delta$ ) for  $x = 0.7, 0.8, 1.1,$  and  $1.9$  samples, which follows the SODS, while the one of the  $x = 1.4$  samples does not. Nonetheless, at temperatures above 600 K, the isomer shift values of  $x = 1.1$  and  $1.9$  samples show an

abrupt change. At such high temperatures, interfacial reactions between the GaAs substrate and Mn<sub>x</sub>Ga films may take place, forming two phase regions of Mn<sub>2</sub>As and MnGa,<sup>[10,48]</sup> thus modifying the hyperfine parameters of the probe atom and therefore  $\delta_\Delta$ . With regard to the quadrupole splitting, its value decreases with increasing temperature in all samples, but without following a well-defined trend (see Figure 6d). This evolution can be ascribed to the random annealing of the implantation-induced strains, which leads to a better ordering of the atomic surrounding of the probe atom.

### 3.3. <sup>119</sup>In/Sn eMS

As clearly evidenced from the <sup>57</sup>Mn eMS (see Section 3.3), the magnetism of off-stoichiometric Mn<sub>x</sub>Ga is intimately connected to the redistribution of Mn at Ga sites. By taking the advantage of <sup>119</sup>Sn-eMS through implantation with parent <sup>119</sup>In radioactive ions, we can directly probe the magnetism at Ga sites, by following the implantation with parent <sup>119</sup>In radioactive ions. **Figure 7** shows the <sup>119</sup>In/Sn-eMS spectra collected for Mn<sub>0.8</sub>Ga and Mn<sub>1.4</sub>Ga samples at RT. The first immediate important result is the very large velocity scale range up to  $30 \text{ mm s}^{-1}$  that is needed to resolve the resonant <sup>119</sup>Sn eMS lines from the samples, as compared with the typically used velocities up to  $\approx 7 \text{ mm s}^{-1}$  in <sup>57</sup>Fe-eMS experiments. The <sup>119</sup>In/Sn emission Mössbauer spectra shown in Figure 7 mimic those observed by Tenhover *et al.*, which was analyzed in terms of a six-line magnetic spectrum.<sup>[49]</sup> In the present work, both <sup>119</sup>In/Sn emission Mössbauer spectra of Mn<sub>0.8</sub>Ga and Mn<sub>1.4</sub>Ga spectra are fitted using a distribution of hyperfine field contributions.

Within the energy resolution achieved in <sup>119</sup>Sn-eMS experiments, there is no hint of any nonmagnetic single-line component, which would contribute to a close to  $0 \text{ mm s}^{-1}$  intensity. The apparent very broad doublet cannot be attributed to a nonmagnetic doublet component because this would mean a quadrupole splitting of about  $\Delta = 20 \text{ mm s}^{-1}$ , which has no physical meaning.<sup>[50]</sup> We therefore conclude that the origin of the observed largely broadened apparent doublet has a magnetic

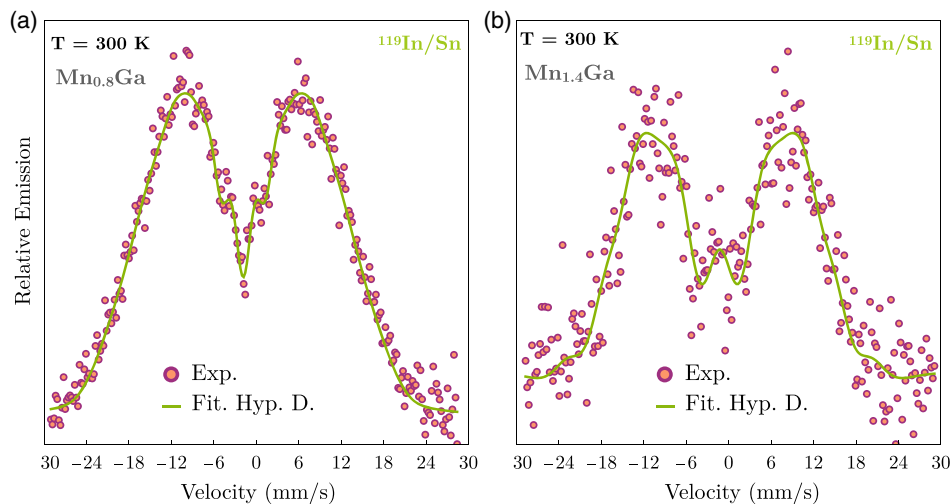


**Figure 7.** <sup>119</sup>In/Sn-eMS spectra for a) Mn<sub>0.8</sub>Ga sample and b) Mn<sub>1.4</sub>Ga sample taken at 300 K. Both spectra are fitted by a single component of hyperfine field distributions.

origin. Indeed, similar largely broadened emission/absorption peaks have been previously reported in PdMnSb samples<sup>[49,51]</sup> and attributed to magnetic hyperfine splitting.

Although the Sn daughter atoms do not possess intrinsic magnetic moment, the neighboring Mn ions can induce a transferred hyperfine field due to the polarization of nonlocalized *s* electrons of the <sup>119</sup>Sn nuclei by the *d* electrons around Mn ions.<sup>[33,39,40]</sup> Within this assumption, the data reported in Figure 7 can be interpreted by using a distribution of magnetically-split sextets with an average hyperfine field values up to 35 T, which is a very large value as induced by the transfer mechanism from neighboring Mn lattice sites. The isomer shift value has been found to be  $\delta = 1.8$  and  $\delta = 1.2$  mm s<sup>-1</sup> for Mn<sub>0.8</sub>Ga and Mn<sub>1.4</sub>Ga, respectively. Moreover, the spectra show no signs of the implantation-induced damage (see Section S1, Supporting Information) or any other component suggesting that <sup>119</sup>In/Sn ions can be located at interstitial sites. Moreover, on grounds of electronegativity it is reasonable to assert that <sup>119</sup>In/Sn are located at substitutional sites, specifically at Ga sites. Although a further temperature dependence study is needed to assert how the hyperfine field revealed by <sup>119</sup>Sn-eMS is linked to the macroscopic magnetism, these results demonstrate the very high magnetic moment transferred to the Ga sites.

The transferred hyperfine field induced at the <sup>119</sup>Sn nuclei is determined by the long-range magnetic order and therefore <sup>119</sup>Sn nuclei are much less sensitive to the strain state as well as to the local distortions induced by the implantation damage than the <sup>57</sup>Fe probe atoms. The observed large hyperfine fields at Ga sites through the hyperfine interactions probed by implanted <sup>119</sup>In/Sn are an elegant direct proof, at most atomic-scale level, for the magnetism in Mn-rich Mn<sub>x</sub>Ga alloys being largely governed by the magnetic polarization of Mn at Ga sites. This further, and strongly, supports the scenario where the AF coupling between neighboring Mn and antisite Mn ions drives the magnitude of *M<sub>s</sub>* as detected by SQUID (see Figure 3) and anticipated in Section 3.3 on the basis of <sup>57</sup>Mn/Fe-eMS. Our results show the suitability of <sup>119</sup>Sn-eMS to probe the magnetic properties of Mn<sub>x</sub>Ga alloys at the most atomic scale, which goes beyond the possibilities that can be achieved with Mn/Fe probes.

Taking into account that the Mn<sub>x</sub>Ga samples are all characterized with a strong PMA (see Figure 3), it is of interest to investigate whether there is any angular dependence<sup>[52]</sup> of the magnetic properties as probed at the most atomic scale by eMS. The experimental procedure and the results are gathered in Section S3, Supporting Information.

While <sup>57</sup>Mn/Fe angular-dependent eMS spectra show little or no angular dependence, in <sup>119</sup>Sn-eMS angular experiments of Mn<sub>0.8</sub>Ga sample (with applied *B<sub>ext</sub>* = 0.6 T), a clear angular dependence is observed. Indeed, the difference spectrum shown at the bottom of Figure S5d, Supporting Information, can be fitted using a single component composed of hyperfine field distribution, with  $\delta = 1.8$  mm s<sup>-1</sup> and maximum hyperfine field value up to 34 T with the intensity ratio of 3:2.4:1. These results are compatible with the values obtained in the spectrum shown in Figure 7a for Mn<sub>0.8</sub>Ga sample, and again compatible with the PMA of the Mn<sub>x</sub>Ga samples as measured by SQUID (see Figure 3).

## 4. Conclusions

The atomic-scale magnetic properties of epitaxial Mn<sub>x</sub>Ga (*x* = 0.7, 0.8, 1.1, 1.4, and 1.9) thin films were studied by <sup>119</sup>Sn and <sup>57</sup>Fe emission Mössbauer measurements following the implantation of parent <sup>119</sup>In and <sup>57</sup>Mn radioactive ions at ISOLDE/CERN. The implanted <sup>57</sup>Mn/Fe species are found to occupy substitutional sites, either at Mn and Ga sites. Most of the implanted ions end up in slightly distorted environments, giving rise to a close to Fe<sup>3+</sup> paramagnetic doublet component. Additionally, two well-distinct magnetically-split sextets Mn<sub>I</sub> and Mn<sub>II</sub> are observed and assigned to the Fe substitution on the Ga and Mn sites, respectively. Both the magnetic contributions are characterized by a relative line intensity ratio being compatible with the macroscopically observed PMA by SQUID measurements. Thanks to the Mn/Ga sites selectivity of the conducted <sup>57</sup>Mn/Fe-eMS analysis, we found a larger magnetic hyperfine field at the Ga site when compared to Mn. Due to the AF coupling existing between the magnetic moments at the Mn and Ga sites, the concentration *x* of the developed Mn<sub>x</sub>Ga thin films is directly tuning their macroscopic magnetic properties. Indeed, our conducted <sup>57</sup>Mn/Fe-eMS experiments reveal that for *x* > 1 the partial reallocation of Mn atoms at Ga sites increases the AF coupling, thus originating an overall lower saturation magnetization in the Mn-rich Mn<sub>x</sub>Ga films when compared to those with *x* < 1. As a matter of fact, there is a monotonous correlation between *x* and the *M<sub>s</sub>*.

We underline how the high sensitivity of <sup>57</sup>Mn/Fe-eMS to the implantation-induced local distortions and/or lattice strain makes the atomic-scale magnetic characterization as conducted through radioactive <sup>57</sup>Mn quite challenging, for instance, preventing to get further insight from angular-dependent measurements. On the other hand, by conducting <sup>119</sup>Sn-eMS we detected very clear magnetic components as due to the large total transferred hyperfine field from polarized *d* conduction electrons of Mn ions at Ga sites. Indeed, even in the presence of strong local distortions, clear angular dependence is observed in the <sup>119</sup>Sn-eMS measurements, demonstrating the substitutional nature of the implanted <sup>119</sup>In/Sn ions at the Ga sites. Our results allowed to get some insights into the intimate correlation between the compositional dependence of the macroscopic magnetic properties of epitaxial L1<sub>0</sub>-Mn<sub>x</sub>Ga thin films with the chemical, structural, and magnetic properties revealed at the most atomic scale through <sup>57</sup>Mn/Fe and <sup>119</sup>In/Sn eMS conducted at ISOLDE/CERN.

## Supporting Information

Supporting Information is available from the Wiley Online Library or from the author.

## Acknowledgements

The work was carried out in the framework of the experiment IS-578 at ISOLDE/CERN and financed by the European Commission through the Horizon 2020 program (grant nos. 654002 and ENSAR 2) and with the support provided by the Federal Ministry of Education and Research (BMBF) through the grant 05K16PGA. I.U. thanks GNT and acknowledges financial support by the Basque Government and Spanish Ministry of

Economy and Competitiveness under grants IT-1005-16, and RTI2018-094683-B-C5 (4,5) (MCIU/AEI/FEDER, UE), respectively. D.V.Z. acknowledges the support by the German Federal Ministry of Education and Research (BMBF) project # 05K19SI. K.B.-R., H.M., and D.N. acknowledge support from the South African National Research Foundation and the Department of Science and Innovation within the SA-CERN programme. H.M. also acknowledges support from the Alexander von Humboldt (AvH) Foundation.

Open Access Funding provided by Consiglio Nazionale delle Ricerche within the CRUI-CARE Agreement.

## Conflict of Interest

The authors declare no conflict of interest.

## Data Availability Statement

The data that support the findings of this study are available from the corresponding author upon reasonable request.

## Keywords

emission Mössbauer spectroscopy, magnetism, MnGa alloys, perpendicular magnetic anisotropy

Received: April 15, 2022  
Published online: May 22, 2022

- [1] H. Kurt, K. Rode, M. Venkatesan, P. Stamenov, J. M. D. Coey, *Phys. Rev. B* **2011**, *83*, 020405.
- [2] L. Zhu, J. Zhao, *Appl. Phys. A* **2013**, *111*, 379.
- [3] B. Balke, G. H. Fecher, J. Winterlik, C. Felser, *Appl. Phys. Lett.* **2007**, *90*, 152504.
- [4] S. Ikeda, K. Miura, H. Yamamoto, K. Mizunuma, H. D. Gan, M. Endo, S. Kanai, J. Hayakawa, F. Matsukura, H. Ohno, *Nat. Mater.* **2010**, *9*, 721.
- [5] D. Betto, Y. C. Lau, K. Borisov, K. Kummer, N. B. Brookes, P. Stamenov, J. M. D. Coey, K. Rode, *Phys. Rev. B* **2017**, *96*, 024408.
- [6] C. Burrowes, N. Vernier, J.-P. Adam, L. Herrera Diez, K. Garcia, I. Barisic, G. Agnus, S. Eimer, Joo-Von Kim, T. Devolder, A. Lamperti, R. Mantovan, B. Ockert, E. E. Fullerton, D. Ravelosona, *Appl. Phys. Lett.* **2013**, *103*, 182401.
- [7] A. Digiacomo, R. Mantovan, N. Vernier, T. Devolder, K. Garcia, G. Tallarida, M. Fanciulli, A. Lamperti, B. Ocker, L. Baldi, M. Mariani, D. Ravelosona, *Phys. Rev. Appl.* **2018**, *10*, 064053.
- [8] H. Sato, E. C. I. Enobio, M. Yamanouchi, S. Ikeda, S. Fukami, S. Kanai, F. Matsukura, H. Ohno, *Appl. Phys. Lett.* **2014**, *105*, 062403.
- [9] L. Zhu, S. Nie, K. Meng, D. Pan, J. Zhao, H. Zheng, *Adv. Mater.* **2012**, *24*, 4547.
- [10] L. J. Zhu, D. Pan, S. H. Nie, J. Lu, J. H. Zhao, *Appl. Phys. Lett.* **2013**, *102*, 132403.
- [11] S. Mizukami, T. Kubota, F. Wu, X. Zhang, T. Miyazaki, H. Naganuma, M. Oogane, A. Sakuma, Y. Ando, *Phys. Rev. B* **2012**, *85*, 014416.
- [12] K. K. Meng, J. Miao, X. G. Xu, Y. Wu, X. P. Zhao, J. H. Zhao, Y. Jiang, *Phys. Rev. B* **2016**, *94*, 214413.
- [13] R. Ranjbar, K. Z. Suzuki, Y. Sasaki, L. Bainsla, S. Mizukami, *Jpn. J. Appl. Phys.* **2016**, *55*, 120302.
- [14] Q. L. Ma, T. Kubota, S. Mizukami, X. M. Zhang, H. Naganuma, M. Oogane, Y. Ando, T. Miyazaki, *Appl. Phys. Lett.* **2012**, *101*, 032402.
- [15] X. Zhao, S. Mao, H. Wang, D. Wei, J. Zhao, *Appl. Phys. Lett.* **2021**, *118*, 092401.
- [16] T. A. Bither, W. H. Cloud, *J. Appl. Phys.* **1965**, *36*, 1501.
- [17] J. Winterlik, B. Balke, G. H. Fecher, C. Felser, M. C. M. Alves, F. Bernardi, J. Morais, *Phys. Rev. B* **2008**, *77*, 054406.
- [18] H. Kurt, K. Rode, M. Venkatesan, P. Stamenov, J. M. D. Coey, *Phys. Status Solidi B* **2011**, *248*, 2338.
- [19] X. Lu, J. Liang, Z. Yang, *Acta Phys. Sin.* **1979**, *28*, 54.
- [20] E. Lu, D. C. Ingram, A. R. Smith, J. W. Knepper, F. Y. Yang, *Phys. Rev. Lett.* **2006**, *97*, 146101.
- [21] J. Winterlik, S. Chadov, A. Gupta, V. Alijani, T. Gasi, K. Filsinger, B. Balke, G. H. Fecher, C. A. Jenkins, F. Casper, J. Kübler, G.-D. Liu, L. Gao, S. S. P. Parkin, C. Felser, *Adv. Mater.* **2012**, *24*, 6283.
- [22] R. Mantovan, R. Fallica, A. Mokhles Gerami, T. E. Møhlholt, C. Wiemer, M. Longo, H. P. Gunnlaugsson, K. Johnston, H. Masenda, D. Naidoo, M. Ncube, K. Bharuth-Ram, M. Fanciulli, H. P. Gislason, G. Langouche, S. Ólafsson, G. Weyer, *Sci. Rep.* **2017**, *7*, 8234.
- [23] R. Mantovan, H. P. Gunnlaugsson, K. Johnston, H. Masenda, T. E. Møhlholt, D. Naidoo, M. Ncube, S. Shayestehaminzadeh, K. Bharuth-Ram, M. Fanciulli, H. P. Gislason, G. Langouche, S. Ólafsson, L. M. C. Pereira, U. Wahl, P. Torelli, G. Weyer, *Adv. Electron. Mater.* **2015**, *1*, 1400039.
- [24] D. V. Zyabkin, U. Vetter, F. M. Linderhof, H. P. Gunnlaugsson, P. Schaaf, *Nucl. Instrum. Methods Phys. Res., Sect. A* **2020**, *968*, 163973.
- [25] H. P. Gunnlaugsson, K. Johnston, T. E. Møhlholt, G. Weyer, R. Mantovan, H. Masenda, D. Naidoo, S. Ólafsson, K. Bharuth-Ram, H. P. Gislason, G. Langouche, M. B. Madsen, *Appl. Phys. Lett.* **2012**, *100*, 042109.
- [26] A. Koebe, T. Shima, M. Doi, *Jpn. J. Appl. Phys.* **2016**, *55*, 07MC04.
- [27] V. Fedoseyev, K. Batzner, R. Catherall, A. Evensen, D. Forkel-Wirth, O. Jonsson, E. Kugler, J. Lettry, V. Mishin, H. Ravn, G. Weyer, *Nucl. Instrum. Methods Phys. Res., Sect. B* **1997**, *126*, 88.
- [28] G. Weyer, *Hyperfine Interact.* **2000**, *129*, 371.
- [29] V. N. Fedoseyev, G. Huber, U. Köster, J. Lettry, V. I. Mishin, H. Ravn, V. Sebastian, *Hyperfine Interact.* **2000**, *127*, 409.
- [30] H. P. Gunnlaugsson, *Hyperfine Interact.* **2016**, *237*, 79.
- [31] H. P. Gunnlaugsson, T. E. Møhlholt, R. Mantovan, H. Masenda, D. Naidoo, W. B. Dlamini, R. Sielemann, K. Bharuth-Ram, G. Weyer, K. Johnston, G. Langouche, S. Ólafsson, H. P. Gislason, Y. Kobayashi, Y. Yoshida, M. Fanciulli, *Appl. Phys. Lett.* **2010**, *97*, 142501.
- [32] Z. Yang, J. Li, D. Wang, K. Zhang, X. Xie, *J. Magn. Magn. Mater.* **1998**, *182*, 369.
- [33] Q. M. Lu, M. Yue, H. G. Zhang, M. L. Wang, F. Yu, Q. Z. Huang, D. H. Ryan, Z. Altounian, *Sci. Rep.* **2015**, *5*, 17086.
- [34] Y. Huh, P. Kharel, V. R. Shah, X. Z. Li, R. Skomski, D. J. Sellmyer, *J. Appl. Phys.* **2013**, *114*, 013906.
- [35] H. Gunnlaugsson, M. Fanciulli, M. Dietrich, K. Bharuth-Ram, R. Sielemann, G. Weyer, the ISOLDE Collaboration, *Nucl. Instrum. Methods Phys. Res., Sect. B* **2002**, *186*, 55.
- [36] G. Weyer, H. P. Gunnlaugsson, M. Dietrich, H. Fynbo, K. Bharuth-Ram, the ISOLDE Collaboration, *Eur. Phys. J. Appl. Phys.* **2004**, *27*, 317.
- [37] G. Weyer, A. Burchard, M. Fanciulli, V. Fedoseyev, H. Gunnlaugsson, V. Mishin, R. Sielemann, *Physica B* **1999**, *273–274*, 363.
- [38] P. Schwalbach, S. Laubach, M. Hartick, E. Kankeleit, B. Keck, M. Menningen, R. Sielemann, *Phys. Rev. Lett.* **1990**, *64*, 1274.
- [39] D. H. Ryan, M. Yue, C. B. Boyer, X. B. Liu, Q. Lu, H. Zhang, C. Li, M. Wang, Z. Altounian, *Sci. Rep.* **2017**, *7*, 646.

- [40] N. Al-Aqtash, R. Sabirianov, *J. Magn. Magn. Mater.* **2015**, 391, 26.
- [41] A. Bedoya Pinto, *PhD Dissertation*, Lima, Peru **2010**.
- [42] P. Lázpita, J. M. Barandiarán, J. Gutiérrez, J. Feuchtwanger, V. A. Chernenko, M. L. Richard, *New J. Phys.* **2011**, 13, 033039.
- [43] I. Unzueta, J. López-García, V. Sánchez-Alarcos, V. Recarte, J. I. Pérez-Landazábal, J. A. Rodríguez-Velamazán, J. S. Garitaonandia, J. A. García, F. Plazaola, *Appl. Phys. Lett.* **2017**, 110, 181908.
- [44] I. Unzueta, J. López-García, V. Sánchez-Alarcos, V. Recarte, J. I. Pérez-Landazábal, J. A. Rodríguez-Velamazán, J. S. Garitaonandia, J. A. García, F. Plazaola, *Metals* **2021**, 11, 450.
- [45] I. Unzueta, J. López-García, V. Sánchez-Alarcos, V. Recarte, J. I. Pérez-Landazábal, J. A. Rodríguez-Velamazán, J. S. Garitaonandia, J. A. García, F. Plazaola, *Hyperfine Interact.* **2018**, 239, 34.
- [46] A. W. Arins, H. F. Jurca, J. Zappellon, J. Varalda, I. L. Graff, W. H. Schreiner, D. H. Mosca, *IEEE Trans. Magn.* **2013**, 49, 5595.
- [47] C. L. Zha, R. K. Dumas, J. W. Lau, S. M. Mohseni, S. R. Sani, I. V. Golosovsky, A. F. Monsen, J. Nogués, J. Akerman, *J. Appl. Phys.* **2011**, 110, 093902.
- [48] J. L. Hilton, B. D. Schultz, S. McKernan, C. J. Palmström, *Appl. Phys. Lett.* **2004**, 84, 3145.
- [49] M. Tenhover, P. Boolchand, *Phys. Rev. B* **1978**, 18, 6292.
- [50] Ada López, I. Souza Azevedo, J. E. Musa, E. Baggio-Saitovitch, S. García García, *Phys. Rev. B* **2003**, 68, 134516.
- [51] P. Boolchand, M. Tenhover, S. Jha, G. Langouche, B. Triplett, S. Hanna, P. Jena, *Phys. Lett. A* **1975**, 54, 293.
- [52] D. R. Vij, *Handbook of Applied Solid State Spectroscopy*, Springer US, New York **2006**.